

# Preparation and Dielectric Properties of Co Contained Unfilled Tungsten Bronze Ceramics Ba<sub>4</sub>RCo<sub>0.5</sub>Nb<sub>9.5</sub>O<sub>30</sub>

**Xiaoying Guo**

Guilin University of Technology

**Weifeng Zhang**

Shenzhen Institute of Information Technology

**Shan Wu**

Guilin University of Technology

**Chaozhong Sun**

Guilin University of Technology

**Changzheng Hu** (✉ [huchzh@foxmail.com](mailto:huchzh@foxmail.com))

Guilin University of Technology <https://orcid.org/0000-0003-1454-9494>

**Laijun Liu**

Guilin University of Technology

**Liang Fang**

Guilin University of Technology

**Nengneng Luo**

Guangxi University

---

## Research Article

**Keywords:** tungsten bronze structure, impedance, dielectric properties, ferroelectrics, ceramics

**Posted Date:** March 16th, 2021

**DOI:** <https://doi.org/10.21203/rs.3.rs-183415/v1>

**License:**  This work is licensed under a Creative Commons Attribution 4.0 International License.

[Read Full License](#)

---

# **Preparation and Dielectric Properties of Co Contained Unfilled Tungsten Bronze Ceramics $\text{Ba}_4\text{RCo}_{0.5}\text{Nb}_{9.5}\text{O}_{30}$**

Xiaoying Guo<sup>a</sup>, Weifeng Zhang<sup>b\*</sup>, Shan Wu<sup>a</sup>, Chaozhong Sun<sup>a</sup>, Changzheng Hu<sup>a\*</sup>,

Laijun Liu<sup>a</sup>, Liang Fang<sup>a</sup>, Nengneng Luo<sup>a,c</sup>

a. Guangxi Key Laboratory of Optical and Electronic Materials and Devices, Key  
Laboratory of New Processing Technology for Nonferrous Metals and Materials,  
Ministry of Education, College of Material Science and Engineering, Guilin  
University of Technology, Guilin 541004, China

b. Department of Electronic and Communication Technology, Shenzhen Institute of  
Information Technology, Shenzhen 518172, China

c. Guangxi Key Laboratory of Processing for Non-Ferrous Metals and Featured  
Materials, Key Laboratory of New Processing Technology for Non-Ferrous Metals  
and Materials, Ministry of Education, School of Resources, Environment and  
Materials, Guangxi University, Nanning, 530004, China

## **Abstract**

In this study,  $\text{Ba}_4\text{RCo}_{0.5}\text{Nb}_{9.5}\text{O}_{30}$  ( $\text{R} = \text{La}, \text{Nd}, \text{Sm}, \text{Eu}$ ) (BRCN) ceramics were synthesized using a high-temperature solid-state reaction. The effects of rare-earth ions with different ionic radii at A sites on the phase structure, microstructure, and dielectric properties of ceramics have been systematically studied. The full profile refinement XRD results show that all ceramic samples are tetragonal tungsten bronze

---

Corresponding author. Tel: 86 773 5896290, E-mail address: [huchzh@foxmail.com](mailto:huchzh@foxmail.com) (C.Z. Hu)

Corresponding author. Tel: 86 755 89226254, E-mail address: [hbwfzhang@163.com](mailto:hbwfzhang@163.com) (W.F. Zhang)

(TTB). As the radius of the rare-earth ions decreases, the relaxation ferroelectric phase transition transforms into the dispersed phase transition, and the frequency dispersion of the ceramic samples gradually decreases. The high-frequency shift of Raman peak indicates that lattice distortion is severe. P-E loops under maximum applied electric field showed that BRCN ceramics can be used for energy storage.

**Keywords:** tungsten bronze structure; impedance; dielectric properties; ferroelectrics; ceramics

## 1. Introduction

The tetragonal tungsten bronze (TTB) structure exist a plurality of ionic positions and has a flexible crystal structure, which has aroused extensive research interest. It is the most striking ferroelectric material after the perovskite structure [1-3]. Ferroelectrics, as an essential functional material, have attracted increased attention and research due to their excellent dielectric, pyroelectric, piezoelectric, and photoelectric properties [4]. The common structure of a TTB is  $(A1)_2(A2)_4(C)_4(B1)_2(B2)_8O_{30}$ . TTB cell is composed of an eight  $BO_6$  octahedron co-corner connection. A-site is usually filled with large-radius ions, B-site generally has a highly coordinated ion filling, and C-site is generally a vacant filling [5-7]. The complex structure of tungsten bronze compounds allows manual manipulation. The lattice structure can be changed by altering the respective proportions of A-site and B-site ions to further change the electrochemical characteristics.

Chen et al. used rare-earth elements ( $Ln = La, Nd, Sm$ ) to replace the A1 site ions of Fe-doped filled tungsten bronze  $Ba_3SrLn_2Fe_2Nb_8O_{30}$  and conducted research on dielectric characteristics. It was found that  $Ba_3SrLn_2Fe_2Nb_8O_{30}$  demonstrates the characteristics of relaxation ferroelectric. When ionic radius decreases, permittivity maximum temperature ( $T_{max}$ ) increases. This is because of the occupancy of different valence and ionic radii in the same position, resulting in the Fe/Nb dipole deviating from the center, and the long-range order at low temperature is disrupted by the distribution field, thus facilitating the formation of relaxor ferroelectrics [8-10]. In this article, we also investigated the influence of A site substitution, but we used Co to

dope B site. Liu et. al. synthesized  $\text{Ba}_6\text{CoNb}_9\text{O}_{30}$  ceramics to indicate nature of the relaxor ferroelectric, a wide dielectric peak and frequency dispersion. The maximum dielectric constant value of  $\text{Ba}_6\text{CoNb}_9\text{O}_{30}$  ceramics is about 100 higher than the  $\text{Ba}_3\text{SrLn}_2\text{Fe}_2\text{Nb}_8\text{O}_{30}$  ceramics as previously reported [8,11]. Guo et. al. have systematically studied  $\text{Ba}_4\text{RFe}_{0.5}\text{Nb}_{9.5}\text{O}_{30}$  ( $\text{R} = \text{La, Nd, Eu, Gd}$ ) and found that the relaxor ferroelectric phase transition characteristics of the ceramics are evident, and the Fe and Nb appropriately occupy the B sites. At the same time,  $\text{Ba}_4\text{RFe}_{0.5}\text{Nb}_{9.5}\text{O}_{30}$  ( $\text{R} = \text{La, Nd, Eu, Gd}$ ) has strong dielectric loss [12-16].

To date, there are few studies on the unfilled TB compound that introduces Co into the B site in tungsten bronze. In this paper,  $\text{Ba}_4\text{RCo}_{0.5}\text{Nb}_{9.5}\text{O}_{30}$  ( $\text{R} = \text{La, Nd, Sm, Eu}$ ) (BRCN) ceramics were synthesized by high-temperature solid-state method. A systematic study was conducted on the influence of rare-earth ions on the phase structure, microstructure, and dielectric properties of the ceramics.

## 2. Experimental procedures

In this experiment, high-purity oxide powders  $\text{BaCO}_3$  (Aladdin, >99.99% purity),  $\text{La}_2\text{O}_3$  (Ansheng >99.99% purity),  $\text{Nd}_2\text{O}_3$  (Ansheng >99.99% purity),  $\text{Sm}_2\text{O}_3$  (Ansheng >99.99% purity),  $\text{Eu}_2\text{O}_3$  (Ansheng >99.99% purity),  $\text{Co}_2\text{O}_3$  (Sinopharm >99.95% purity), and  $\text{Nb}_2\text{O}_5$  (Conghua >99.99% purity) were used as experimental material.  $\text{Ba}_4\text{RCo}_{0.5}\text{Nb}_{9.5}\text{O}_{30}$  ( $\text{R} = \text{La, Nd, Sm, Eu}$ ) ceramics were successfully synthesized by high-temperature solid-phase reaction. The unmixed powders were ball-milled in nylon jars with zirconia balls for 8 h, dried and pressed

into a column, then calcined for 6 h at 1423 K. After secondary ball milling, 5 wt % polyvinyl alcohol was added as a binder to the pre-fired powder. After sieving, they were placed in a 5-mm radius pillar with and pressed into sheets of 1 mm thickness at 100 MPa. The sample was heated at 823 K for 4 h, enabling PVA discharge from the sample. Then, in order to obtain dense ceramics, the ceramics were sintered for 6h at 1553-1573 K. The two sides of the sintered ceramics were polished and coated with silver paste, then heated at 923 K for 30 min.

The actual density of the ceramic obtained was calculated using the Archimedes method. The ceramics were characterized by PNalytical X'Pert PRO powder diffractometer (XRD) ( $\lambda_{\text{CuK}\alpha} = 1.5406 \text{ \AA}$ ). The Hitachi S-4800 field emission scanning electron microscope (SEM) was used to observe the micro-morphology of the ceramic surface. The Raman spectrum of the ceramics was obtained using the DXR laser confocal microscope (Raman spectrometer, Thermo Fisher Scientific). The laser source was a 532 nm incident light source generated by an Ar ion laser. The Agilent 4294A precision impedance analyzer with TZDM-200-300 temperature control system was used to obtain the dielectric constant and dielectric loss of Ba<sub>4</sub>RCo<sub>0.5</sub>Nb<sub>9.5</sub>O<sub>30</sub> ceramics at different frequencies (100 Hz to 1 MHz) and at varying temperatures (98 K to 523 K). The alternating current (AC) impedance spectra of ceramic Ba<sub>4</sub>RCo<sub>0.5</sub>Nb<sub>9.5</sub>O<sub>30</sub> were tested using Agilent 4294A precision impedance analyzer.[17]. A Radian Precision 10 kV HVI-SC analyzer was used to measure the room-temperature P-E hysteresis loops and I-E curves.

### **3. Results and discussion**

We used Fullprof software to refine the XRD diagram of BRCN ceramics, and the results are shown in Fig. 1(a)-(d). It can be seen that rare-earth ions and Ba<sup>2+</sup> ions occupy A1-sites and A2-sites, respectively, while Co<sup>3+</sup> and Nb<sup>5+</sup> ions occupy B1-sites and B2-site positions randomly. The main crystal phase of all ceramic samples is a TTB structure. We calculated the cell parameters and R factor values as shown in Table 1. Then the crystallographic information file (cif) of the structure was used to draw the cell structure, as shown in Fig. 1(e). As the radius decrease of the substituted rare-earth ions, the volume of the crystal cell decreases gradually. Table 2 lists the tolerance factor and electronegativity of the ceramics as calculated. A decrease in the radius of the rare-earth ion leads to a gradual decrease in the A1 tolerance factor, the overall tolerance factor, and the electronegativity difference of the BRCN ceramics. The closer the tolerance factor is to 1 and the smaller the electronegativity, the more stable the structure. Therefore, the decrease in radius of rare-earth ions results in reduced stability of Co-substituted tungsten bronze structural ceramics.

Fig. 2(a)-(d) are SEM images of BRCN ceramics as-sintered surface. As the ionic radius decreases, their apparent size decreases slightly. The figure shows that the surface grains of all samples are closely packed columnar grains, indicating that all samples have good compactness, which is also related to their dielectric properties. The tested densities of all the samples are 5.44, 5.60, 5.50, and 5.54 g.cm<sup>-3</sup>. Moreover, the relative densities of the Ba<sub>4</sub>LaCo<sub>0.5</sub>Nb<sub>9.5</sub>O<sub>30</sub> (BLCN), Ba<sub>4</sub>NdCo<sub>0.5</sub>Nb<sub>9.5</sub>O<sub>30</sub> (BNCN), Ba<sub>4</sub>SmCo<sub>0.5</sub>Nb<sub>9.5</sub>O<sub>30</sub> (BSCN), and Ba<sub>4</sub>EuCo<sub>0.5</sub>Nb<sub>9.5</sub>O<sub>30</sub> (BECN) ceramics are 97.7%, 99.6%, 97.7%, and 98.1%, respectively.

Fig. 3 shows the relationship between the relative dielectric constant ( $\varepsilon_r$ ) and the dielectric loss ( $\tan\delta$ ) of BRCN ceramics in the 40 Hz-1 MHz range at room temperature with frequency. As the ion radius decreases, the frequency stability of its dielectric constant decreases. The dielectric constant of all ceramic samples decreases as the test frequency increases; the dielectric constant of two samples of R = Sm and R = Eu decreases more obviously than that of R = La and R = Nd. There is even a trend below BLCN and BNCN. At low frequencies, different types of polarization, such as atomic polarization, dipole polarization, ion polarization, Maxwell-Wagoner polarization, and electron polarization, affect the dielectric properties of ceramics; thus the relative dielectric constant is large [17,18]. As the frequency increases, the relative dielectric constant gradually decreases and eventually stabilizes. This is because the electron polarization mechanism plays a leading role in the high-frequency region, while other polarization mechanisms are unable to keep up with the changes of external high-frequency alternating electric field. They are unable to respond, leading to the weakening of the contribution of the dielectric constant [14].

The dielectric constant and loss of BRCN ceramics related to different frequencies (100 Hz, 1 kHz, 10 kHz, 100 kHz, and 1 MHz) have been clearly shown in Fig. 4. With the increase of temperature, the dielectric constant at a low frequency is relatively unstable, and the frequency dispersion phenomenon occurs at high temperature. The dielectric behavior of ceramics is evidently affected by the radius of the A1 position ionic radius. The temperature of the maximum dielectric constant ( $T_m$ )

of BLCN and BECN ceramics differs by more than 100 K. As the radius of rare-earth ions decreases, the dielectric constant peak shows a wider relaxation peak. The decrease of the ionic radius will not only cause the change of the lattice structure, but also increase the ion oscillation space inside the BO<sub>6</sub> octahedron [19], as  $T_m$  of all samples gradually move toward higher temperature. In addition, when the temperature rises, the dipoles in the ceramics gradually unify under the action of external electric field torque [20], which will aggravate the collision between the dipoles and lead to an increase in conductance loss. Some studies have shown that the appearance of dielectric loss is also related to the thermal activation energy of carriers [13]. Table 3 lists the relative permittivity and corresponding temperature of the dielectric constant peaks of by BRCN ceramics measured at specific frequencies (10 kHz, 100 kHz, and 1 MHz).

In order to make the abnormal dielectric peak more significant, we focus on the dielectric constant of the BRCN ceramics measured at the test frequency of 1 MHz and the temperature range of 101-523 K, also using used the Curie-Weiss law (Eq. (1)) [21] to fit in Fig. 5:

$$\varepsilon_r = C/(T - T_0) \quad (1)$$

where  $C$  is the Curie-Weiss constant and  $T_0$  is the Curie-Weiss temperature. The Curie-Weiss constants  $C'$  and  $C$  reflect the slope of the reciprocal of the dielectric constant below and above  $T_m$  as temperature change. As shown in Fig. 5, the  $C$  values of BLCN, BNCN, BSCN, and BECN ceramic samples are  $0.862 \times 10^5$ ,  $0.532 \times 10^5$ ,

$0.437 \times 10^5$ , and  $0.467 \times 10^5$ , respectively. Their order of magnitude is close to  $10^5$ , indicating that all samples are displacements of ferroelectrics [22]. Under normal circumstances, the ratio of  $C/C'$  greater than 4 is the first-order ferroelectric phase transition, while less than 4 is usually the second-order ferroelectric phase transition. The  $C/C'$  values of BRCN ceramics were 2.19, 2.60, 2.36, and 1.81, respectively, indicating that all specimens presented second-order ferroelectric phase transition characteristics similar to BRCN ceramics. Additionally, BLCN, BNCN, BSCN, and BECN ceramic samples' dielectric constant fitting reciprocals deviate from the Curie-Weiss law at 251.54 K, 269.01 K, 303.45 K, and 335.92 K, respectively. These four temperatures that deviate from  $T_m$  are defined as the Burns temperature ( $T_B$ ) [23]. A deviation from temperature is generally considered to occur in a range below the  $T_B$ , which is likely due to the structural fluctuations caused by the ionic vibrations of polarization in tungsten bronze ceramics. This disrupts the long-range order of the dipoles, resulting in strong fluctuations in the nanometer microzone, and hence the dielectric constant curve deviates from Curie's law.

Based on the results of the above analysis, we infer that when the temperature rises to the vicinity of the Burns temperature, the dielectric constant curve begins to deviate from the Curie-Weiss law. This signifies that there is a dispersion phenomenon in the dielectric constant peak of BRCN ceramics. To further investigate explore this dispersion phenomenon, we can obtain the dispersion index ( $\gamma$ ) through the revised Curie-Weiss law [24], and the formula is:

$$\ln\left(\frac{1}{\varepsilon} - \frac{1}{\varepsilon_m}\right) = \gamma \ln(T - T_m) + C \quad (2)$$

where  $\varepsilon_r$  is the dielectric constant,  $\varepsilon_m$  is the maximum value of the dielectric constant, and  $C$  is the Curie constant. Fig. 6 (a)-(d) show the functional relationship between  $\ln(1/\varepsilon - 1/\varepsilon_m)$  and  $\ln(T - T_m)$  of BRCN ceramics at 1 MHz frequency. As shown in the figure, the  $\gamma$  values were obtained from Eq. (2), which are 1.38, 1.46, 1.69, and 1.71, respectively.  $\gamma$  value is between 1 and 2. When  $\gamma=1$ , the said ceramics belong to normal ferroelectrics, and when  $\gamma = 2$ , the said ceramics are ideal relaxor ferroelectric ceramics. When the radius of rare-earth ions increases in the A-sites' substitution, BRCN ceramics'  $\gamma$  value increases gradually, exhibiting an increase in the dispersion degree of the sample.

Whether the dielectric properties are related to the crystal grains can be explained through a precise impedance analysis [25]. It is an excellent method to test the electrical properties of tungsten bronze structure, and it simulates the equivalent circuit by using grain and grain boundary and electrode contact surface. The response of a single volume element can be described using a semicircular arc [26]. We use AC impedance plots to measure and analyze the contribution of charge transport at different rare-earth ions of ceramics. All the semicircular arcs in Fig. 7 are below the x-axis, which demonstrates exhibits that in the frequency range of our study, the relaxation is one of non-Debye [27,28]. This indicates that dielectric properties are not affected by both grain and grain boundary.

Fig. 8 (a)-(d) shows the BRCN ceramics normalized at different temperatures of

the imaginary part of impedance ( $Z''$ ) change with the frequency curve. As shown in Fig. 8 (a)-(d), the curves of the normalized imaginary parts of the impedance at different temperatures vary with the frequency, exhibiting the symmetric peak with the largest peak, and the corresponding frequency of the symmetric peak is the relaxation frequency. When the temperature increases, the normalized peak shifts to the high-frequency direction, indicating that the relaxation experienced by all samples is the relaxation behavior of thermal activation. This may be due to the free transport of carriers and the space charge in grain boundaries causing the carrier transition between adjacent lattice points. Researchers use the Arrhenius equation (Eq. (3)) to describe the relationship between relaxation frequency and temperature [29,30]:

$$f_{max} = f_0 \exp(-E_{rel}/k_B T) \quad (3)$$

where  $f_0$  is the pre-factor,  $E_{rel}$  is the relaxation activation energy, and  $k_B$  refers to Boltzmann constant. As shown in Fig. 8 (e), the relaxation activation energies of BRCN ceramics are 0.87 eV, 0.83 eV, 0.81 eV, and 0.91 eV, respectively, through the linear fitting of Arrhenius equation.

Fig. 9 (a)-(d) shows the relationship, using a diagram among the AC conductance of BRCN ceramics that change with frequency at four specific temperatures. From the graph we could determine that the AC conductance of all samples demonstrate a dispersion phenomenon moving toward higher frequency with the increase of test temperature. Furthermore, we can see that the AC conductance of all ceramic samples decreases with the decrease of frequency, and eventually it tends to be stable at a

specific frequency, almost unchanged. This indicates that direct current (DC) conductance is dominant at this time. In the specific temperature change and frequency range, the relationship between conductance and frequency follows the "dielectric universal response" (UDR) rule [31]. The formula is:

$$\sigma_{ac} = \sigma_{dc} + A\omega^n \quad (0 < n < 1) \quad (4)$$

where  $\sigma_{ac}$  is the DC conductance,  $A$  is the temperature-dependent constant,  $\omega$  is the frequency, and  $n$  is the exponent dependent on frequency and temperature. This formula describes the processes and phenomena of the interaction between dipoles and charges. Therefore, the relationship between DC conductance and temperature also follows the equation (Eq. (5)) [32]:

$$\sigma_{dc} = \sigma_0 \exp(-E_{dc}/k_B T) \quad (5)$$

where  $\sigma_0$  is the pre-factor,  $E_{dc}$  is the activation energy of DC conductivity, and  $k_B$  is the Boltzmann constant. As shown in Fig. 9 (e), we have obtained the DC conductance activation energy of BRCN ceramics by 0.82 eV, 0.76 eV, 0.74 eV, and 0.83 eV by using Arrhenius equation. The change trend of the DC conductance activation energy of all ceramics keeps up with the relaxation activation energy: as the radius of rare-earth ions decreases, the DC conductance activation energy first increases and then decreases. The DC conductance activation energy is caused by the generation of charge carriers and the long-range migration or hopping of charge carriers; however, the relaxation activation energy is caused by the carrier migration and transition between adjacent lattices. According to relevant literature, the

activation energy induced by ionization of oxygen vacancies in ceramics at high temperature is approximately 0.3-0.5 eV, and the activation energy caused by ionization of double ionization oxygen vacancies is approximately 0.6-1.2 eV. Therefore, the activation energy of BRCN ceramics is likely caused by ionization of double ionization oxygen vacancies [33,34]. When metal oxides are sintered at high temperature in air, oxygen vacancies are readily formed from oxygen loss in the lattice. The Kröger-Vink defect equations explain the generation mechanism of oxygen vacancies [35]:



However, the valence state of  $Co^{3+}$  ions in ceramic samples is unstable; they could be combined with the electrons generated in the Eqs. (6a)-(6c) process to form  $Co^{3+}$ . As the radius of the rare-earth ions substituted by the A1-sites decreases, the relaxation activation energy of BRCN ceramics has the same change trend as the DC conductance activation energy, and both increase first and then decrease. We assumed that whether or not it is related to the concentration of oxygen vacancies, the phenomenon shows that the result is positive.

The ceramics' room temperature Raman spectra are shown in Fig. 10, wavenumber is in the range of  $50-1200\text{ cm}^{-1}$ . As shown in Fig. 10, all samples' Raman spectra are similar, with three characteristic peaks near 250, 630, and 840

$\text{cm}^{-1}$ . According to the relevant literature, typical TTB compounds have two vibration modes near the Raman peaks: the O-B-O bending vibration mode ( $v_5$ ) exists at  $250 \text{ cm}^{-1}$  and the B-O stretching vibration mode ( $v_2$  and  $v_1$ ) exists at  $630$  and  $840 \text{ cm}^{-1}$ . When the wave number is less than  $200 \text{ cm}^{-1}$ , the Raman displacement is related to the movement of  $\text{Ba}^{2+}$  ions, which is the  $\text{BO}_6$  octahedron external vibration mode. When the wave number is greater than  $200 \text{ cm}^{-1}$ , the Raman displacement is related to the internal vibration mode of the octahedron [36]. As the radius of A1 rare-earth ions decreases, the corresponding peaks of the characteristic Raman peaks of BRCN ceramics are  $623.6004 \text{ cm}^{-1}$ ,  $624.5646 \text{ cm}^{-1}$ ,  $625.0468 \text{ cm}^{-1}$ , and  $625.5689 \text{ cm}^{-1}$ . The blue shift of Raman spectroscopy confirms that the change of the rare-earth ions will lead to the enhancement of the interaction force between the external atoms and the central atoms of the  $\text{BO}_6$  octahedron. The influence of A ions on the distortion of  $\text{BO}_6$  octahedron will evolve into a significant effect on the electrical properties of the ceramics. The change of the ion radius at A-site will cause a  $\text{BO}_6$  octahedral distortion, which will affect the electrical properties of tungsten bronze ceramics.

Fig. 11 (a) shows the P-E curve under maximum applied electric field ( $E_{\max}$ ). As predicted, the ferroelectric response of all samples is given. The calculated residual polarization ( $P_r$ ) values of BLCN, BNCN, BSCN, and BECN are  $0.470$ ,  $0.766$ ,  $0.838$ , and  $1.038 \mu\text{C.cm}^{-2}$ , respectively, showing that they undergo a macroscopic polarization process under  $E_{\max} \leq 80 \text{ kV cm}^{-1}$ , which is indispensable to the location and radius of ions under nanometer size. The polarization phenomenon is evident with

the decrease of the radius of rare-earth ions. We found that, at a slightly lower electric field intensity, the hysteresis loop presents a straight line, and the saturation polarization ( $P_{\max}$ ) value is low, indicating that the energy storage density is low at low electric field intensity. Therefore, we used the highest electric field to study the energy storage density and efficiency. We use Eqs. (7a)-(7c) to calculate them, as shown in Fig. 11 (b) [37]; the highest energy storage density is  $0.15 \text{ J.cm}^{-3}$  and the energy storage efficiency is 64%-77%.

$$\text{Energy storage density: } W_{st} = \int_0^{P_m} EdP \quad (7a)$$

$$\text{Recoverable energy density: } W_{rec} = \int_{P_r}^{P_m} EdP \quad (7b)$$

$$\text{Energy storage efficiency: } \eta = \frac{W_{rec}}{W_{st}} \times 100\% \quad (7c)$$

#### 4. Conclusions

$\text{Ba}_4\text{RCo}_{0.5}\text{Nb}_{9.5}\text{O}_{30}$  ( $\text{R} = \text{La, Nd, Sm, Eu}$ ) unfilled tungsten bronze structural ceramics were prepared by high-temperature solid-state synthesis. The effects of different rare-earth ions on the phase structure, microstructure, and dielectric properties of ceramics were studied. Room-temperature XRD analysis showed that the tetragonal unfilled TB structure in space group  $P4bm$  is obtained for BRCN ceramics, rare-earth ions occupying A1 sites. With the decrease of the radius of rare-earth ions substituted by A1 sites, vital frequency dispersion phenomena were observed, demonstrating typical relaxor ferroelectric phase transition characteristics. This may be due to the distortion of  $\text{BO}_6$  octahedron. Through high-temperature impedance analysis, it was determined that the ceramics undergo thermal activation

relaxation behavior, with the relaxation activation energy first increasing and then decreasing. At the same time, the activation energy of DC conductance after fitting into the Arrhenius equation also increases first and then decreases. They are all related to double ionized oxygen vacancies. Raman spectroscopy analyzes BRCN ceramics structure and shows Raman peaks shift to high wave numbers as the radius of rare-earth ions decreases, indicating that the distortion of  $\text{BO}_6$  octahedron is slightly increased. The P-E curves show that their  $P_r$  is approximately  $0.5\text{-}1 \mu\text{C.cm}^{-2}$ , the energy storage efficiency is 64%-77%, and the highest energy storage density is  $0.15 \text{ J.cm}^{-3}$ .

## Acknowledgments

All the authors thank the National Natural Science Foundation of China (11564009), Natural Science Foundation of Guangxi (2018GXNSFAA050010, 2019GXNSFGA245006), high-level innovation team and outstanding scholar program of Guangxi institutes, and open funding of the Key Laboratory of New Processing Technology for Nonferrous Metal & Materials, Ministry of Education/Guangxi Key Laboratory of Optical and Electronic Materials and Devices (19AA-15, 20KF-16) for financial support.

## References

- [1] K. Lin, Z.Y. Zhou, L.J. Liu, H.Q. Ma, J. Chen, J.X. Deng, J.L. Sun, L. You, H. Kasai, K. Kato, M. Takata, X.R. Xing, *J. Am. Chem. Soc.* **137**, 13468-13471 (2015).
- [2] T.T. Gao, W. Chen, X.N. Zhu, X.L. Zhu, X.M. Chen, *Mater. Chem. Phys.* **181**, 47-53 (2016).
- [3] X.L. Zhu, K. Li, X.M. Chen, *J. Am. Ceram. Soc.* **97**, 329-338 (2014).
- [4] C.Z. Hu, X.Y. Peng, C.C. Li, L. Fang, L.J. Liu, *Ferroelectrics*. **404**, 33-38(2010).
- [5] A. Simon, J. Ravez, *C. R. Chimie*. **9**, 1268-1276 (2006).
- [6] J.S. Hong, Y.H. Huang, X.Q. Liu, J. L, Y.J. Wu, *J. Alloy. Compd.* **775**, 1199-1205 (2019).
- [7] M.L. Zhang, X.Z. Zuo, *J. Alloy. Compd.* **806**, 386-392 (2019).
- [8] W. Chen, W.Z. Yang, X.Q. Liu, X.M. Chen, *J. Alloy. Compd.* **675**, 311-316 (2016).
- [9] M. Josse, O. Bidault, F. Roulland, E. Castel, A. Simon, D. Michau, R.V. Mühll, O.Nguyen, M. Maglione. *Solid State Sci.* **11**, 1118-1123 (2009),
- [10] G.Z. Li, Z. Chen, X.J. Sun, L.J. Liu, L. Fang, B. Elouadi, *65*, 260-265 (2015).
- [11] P.P. Liu, X.L. Zhu, X.M. Chen, *J. Appl. Phys.* **106**, 074111 (2009).
- [12] Z. Guo, S. Wu, C.Z. Hu, L.J. Liu, L. Fang, *J. Alloy. Compd.* **773**, 470-481 (2018).

- [13] C.Z. Hu, Z. Guo, S. Wu, Z. Sun, C.C. Li, L.J. Liu, L. Fang, *Ceram. Int.* **44**, 224-227 (2018).
- [14] Z. Guo, Q.H. Zhu, S. Wu, C.Z. Hu, L.J. Liu, L. Fang, *Ceram. Int.* **44**, 7700-7708 (2018).
- [15] C.Z. Hu, Q.H. Zhu, Z. Guo, Z. Sun, L.J. Liu, L. Fang, *J. Wuhan. Univ. Technol.* **32**, 904-909 (2017).
- [16] C.Z. Hu, Z. Sun, Q.H. Zhu, F.Q. Lu, C.C. Li, L.J. Liu, L. Fang, *Ceram. Int.* **42**, 14999-15004 (2016).
- [17] C.Z. Hu, Z. Sun, Q.H. Zhu, L. Fang, L.J. Liu, *J. Mater. Sci. Mater. Electron.* **26**, 515-520 (2015).
- [18] X.M. Chen, Y.H. Sun, X.H. Zheng, *J. Eur. Ceram. Soc.* **23**, 1571-1575 (2003).
- [19] P. Yang, B. Yang, S.L. Hao, L.L. Wei, Z.P. Yang, *J. Alloy. Compd.* **685**, 175-185 (2016).
- [20] C.J. Huang, K. Li, X.Q. Liu, X.L. Zhu, X.M. Chen, *J. Am. Ceram. Soc.* **97**, 507-512 (2014).
- [21] W.B. Feng, X.L. Zhu, X.Q. Liu, M.S. Fu, X. Ma, S.J. Jia, X.M. Chen, *J. Am. Ceram. Soc.* **101**, 1623-1631 (2018).
- [22] G. Zerihun, G.S. Gong, S. Huang, S.L. Yuan, *J. Appl. Phys.* **16**, 843-849 (2016).
- [23] W.C. Liu, W. Zhou, R. Sooryakumar, C.L. Mak, *J. Raman. Spectrosc.* **43**, 326-330 (2012).

- [24] B. Yang, S.L. Hao, P. Yang, L.L. Wei, Z.P. Yang, Ceram. Int. **44**, 8832-8841 (2018).
- [25] B.N. Parida, P.R. Das, R. Padhee, S. Behera, R.N.P. Choudhary, J Mater. Sci: Mater Electron. **25**, 2618-2626 (2014).
- [26] X.H. Li, X.M. Wang, Y.F. Han, X.P. Jing, X.R. Xing, Q.Z. Huang, X.J. Kuang, Q.L. Gao, J. Chen, X.R. Xing, Chem. Mater. **29**, 1989-1993 (2017).
- [27] F.Q. Tao, X.M. Wang, M.L. Gong, F.Q. Lu, M. Allix, X.J. Kuang, L. Fang, J. Am. Ceram. Soc. **100**, 1212-1220 (2017).
- [28] J. Cao, X.J. Kuang, M. Allix, C. Dickinson, J.B. Claridge, M.J. Rosseinsky, D.M. Iddles, Q. Su, Chem. Mater. **23**, 5058-5067 (2011).
- [29] C.Z. Hu, L.J. Hou, L. Fang, L.J. Liu, J. Alloy. Compd. **581**, 547-552 (2013).
- [30] S.F. Liu, Y.J. Wu, J. Li, X.M. Chen, Appl. Phys. Lett. **104**, 082912 (2014).
- [31] J.M. Deng, L.J. Liu, X.J. Sun, S.S. Liu, T.X. Yan, L. Fang, B. Elouadi, Mater. Res. Bull. **88**, 320-329 (2017).
- [32] X.J. Sun, J.M. Deng, L.J. Liu, S.S. Liu, D.P. Shi, L. Fang, B. Elouadi, Mater. Res. Bull. **73**, 437-445 (2016).
- [33] L.J. Liu, Y.M. Huang, C.X. Su, L. Fang, M.X. Wu, C.Z. Hu, H.Q. Fan, Appl. Phys. A, **104**, 1047-1051 (2011).
- [34] L. Cao, Y. Yuan, B. Tang, E.Z. Li, S.R. Zhang, J. Eur. Ceram. Soc. **40**, 12999 (2020).

- [35] S. Wu, C.Z. Sun, X.F. Yang, C.Z. Hu, L.J. Liu, L. Fang, Ceram. Int. **46**, 9240-9248 (2020).
- [36] B. Yang, J.H. L, P. Yang, L.L. Wei, Z.P. Yang, Mater. Chem. Phys. **243**, 122006 (2020).
- [37] H.J. Yang, Z.L. Lu, L.H. Li, W.C. Bao, H.F. J, J.L. Li, A. Feteira, F.F. Xu, Y. Zhang, H.J. Sun, Z.C. Huang, W.C. Lou, K.X. Song, S.K. Sun, G. Wang, D.W. Wang, L.M. Reaney, ACS. Appl. Mater. Inter, **12**, 43942-43949 (2020).

## Figure Captions

**Fig.1** Refinement results of the (a) Ba<sub>4</sub>LaCo<sub>0.5</sub>Nb<sub>9.5</sub>O<sub>30</sub>, (b) Ba<sub>4</sub>NdCo<sub>0.5</sub>Nb<sub>9.5</sub>O<sub>30</sub>, (c) Ba<sub>4</sub>SmCo<sub>0.5</sub>Nb<sub>9.5</sub>O<sub>30</sub>, (d) Ba<sub>4</sub>EuCo<sub>0.5</sub>Nb<sub>9.5</sub>O<sub>30</sub> ceramics. (e) The *ab* and *ac* schematic representation of tetragonal tungsten bronze structure.

**Fig.2** SEM images of the (a) Ba<sub>4</sub>LaCo<sub>0.5</sub>Nb<sub>9.5</sub>O<sub>30</sub>, (b) Ba<sub>4</sub>NdCo<sub>0.5</sub>Nb<sub>9.5</sub>O<sub>30</sub>, (c) Ba<sub>4</sub>SmCo<sub>0.5</sub>Nb<sub>9.5</sub>O<sub>30</sub>, (d) Ba<sub>4</sub>EuCo<sub>0.5</sub>Nb<sub>9.5</sub>O<sub>30</sub> ceramics.

**Fig.3** Frequency dependence dielectric properties of the Ba<sub>4</sub>RCo<sub>0.5</sub>Nb<sub>9.5</sub>O<sub>30</sub> (R = La, Nd, Sm, Eu) ceramics.

**Fig.4** Temperature dependence of dielectric constant ( $\varepsilon_r$ ) and dielectric loss (tan $\delta$ ) of the (a) Ba<sub>4</sub>LaCo<sub>0.5</sub>Nb<sub>9.5</sub>O<sub>30</sub>, (b) Ba<sub>4</sub>NdCo<sub>0.5</sub>Nb<sub>9.5</sub>O<sub>30</sub>, (c) Ba<sub>4</sub>SmCo<sub>0.5</sub>Nb<sub>9.5</sub>O<sub>30</sub>, and (d) Ba<sub>4</sub>EuCo<sub>0.5</sub>Nb<sub>9.5</sub>O<sub>30</sub> ceramics.

**Fig.5** Curie-Weiss fitting of dielectric constant of the (a) Ba<sub>4</sub>LaCo<sub>0.5</sub>Nb<sub>9.5</sub>O<sub>30</sub>, (b) Ba<sub>4</sub>NdCo<sub>0.5</sub>Nb<sub>9.5</sub>O<sub>30</sub>, (c) Ba<sub>4</sub>SmCo<sub>0.5</sub>Nb<sub>9.5</sub>O<sub>30</sub>, and (d) Ba<sub>4</sub>EuCo<sub>0.5</sub>Nb<sub>9.5</sub>O<sub>30</sub> ceramics measured at 1 MHz (experimental data: symbols; fitting result: lines).

**Fig.6** The Vogel-Fulcher fittings of  $\ln(1/\varepsilon - 1/\varepsilon_m)$  as a function of  $\ln(T - T_m)$  for the (a) Ba<sub>4</sub>LaCo<sub>0.5</sub>Nb<sub>9.5</sub>O<sub>30</sub>, (b) Ba<sub>4</sub>NdCo<sub>0.5</sub>Nb<sub>9.5</sub>O<sub>30</sub>, (c) Ba<sub>4</sub>SmCo<sub>0.5</sub>Nb<sub>9.5</sub>O<sub>30</sub>, and (d) Ba<sub>4</sub>EuCo<sub>0.5</sub>Nb<sub>9.5</sub>O<sub>30</sub> ceramics.

**Fig.7** Complex impedance plots of the (a) Ba<sub>4</sub>LaCo<sub>0.5</sub>Nb<sub>9.5</sub>O<sub>30</sub>, (b) Ba<sub>4</sub>NdCo<sub>0.5</sub>Nb<sub>9.5</sub>O<sub>30</sub>, (c) Ba<sub>4</sub>SmCo<sub>0.5</sub>Nb<sub>9.5</sub>O<sub>30</sub>, and (d) Ba<sub>4</sub>EuCo<sub>0.5</sub>Nb<sub>9.5</sub>O<sub>30</sub> ceramics at different temperatures.

**Fig.8** Normalized imaginary parts,  $Z''/Z''_{max}$  of impedance at different frequency for the (a)  $\text{Ba}_4\text{LaCo}_{0.5}\text{Nb}_{9.5}\text{O}_{30}$ , (b)  $\text{Ba}_4\text{NdCo}_{0.5}\text{Nb}_{9.5}\text{O}_{30}$ , (c)  $\text{Ba}_4\text{SmCo}_{0.5}\text{Nb}_{9.5}\text{O}_{30}$ , and (d)  $\text{Ba}_4\text{EuCo}_{0.5}\text{Nb}_{9.5}\text{O}_{30}$  ceramics. (e) Arrhenius plots of the relaxation frequencies ( $f_{max}$ ) of the  $\text{Ba}_4\text{RCo}_{0.5}\text{Nb}_{9.5}\text{O}_{30}$  ( $\text{R} = \text{La, Nd, Sm and Eu}$ ) ceramics. experimental data: symbols; fitting result: lines.

**Fig.9** AC conductivity ( $\sigma_{ac}$ ) at different temperatures of the (a)  $\text{Ba}_4\text{LaCo}_{0.5}\text{Nb}_{9.5}\text{O}_{30}$ , (b)  $\text{Ba}_4\text{NdCo}_{0.5}\text{Nb}_{9.5}\text{O}_{30}$ , (c)  $\text{Ba}_4\text{SmCo}_{0.5}\text{Nb}_{9.5}\text{O}_{30}$ , and (d)  $\text{Ba}_4\text{EuCo}_{0.5}\text{Nb}_{9.5}\text{O}_{30}$  ceramics; the frequency dependence of the (e) DC conductivity ( $\sigma_{dc}$ ) obtained from fitting universal Arrhenius to the AC conductivity.

**Fig.10** Raman spectra of the  $\text{Ba}_4\text{RCo}_{0.5}\text{Nb}_{9.5}\text{O}_{30}$  ( $\text{R} = \text{La, Nd, Sm and Eu}$ ) ceramics at room temperature.

**Fig.11** (a) P-E curve of  $\text{Ba}_4\text{RCo}_{0.5}\text{Nb}_{9.5}\text{O}_{30}$  ( $\text{R} = \text{La, Nd, Sm and Eu}$ ) ceramics under maximum field strength. (b) Energy storage efficiency and energy storage density of ceramics.

## **Table captions**

**Table 1.** Cell parameters and reliability factors of  $\text{Ba}_4\text{RCO}_{0.5}\text{Nb}_{9.5}\text{O}_{30}$  ( $\text{R} = \text{La, Nd, Sm}$  and  $\text{Eu}$ ).

**Table 2.** Tolerance factor and electronegativity difference of  $\text{Ba}_4\text{RCO}_{0.5}\text{Nb}_{9.5}\text{O}_{30}$  ( $\text{R} = \text{La, Nd, Sm and Eu}$ ) ceramics.

**Table 3.** Temperature and value of dielectric constant peak of  $\text{Ba}_4\text{RCO}_{0.5}\text{Nb}_{9.5}\text{O}_{30}$  ( $\text{R} = \text{La, Nd, Sm and Eu}$ ) ceramics at various test frequencies.

# Figures

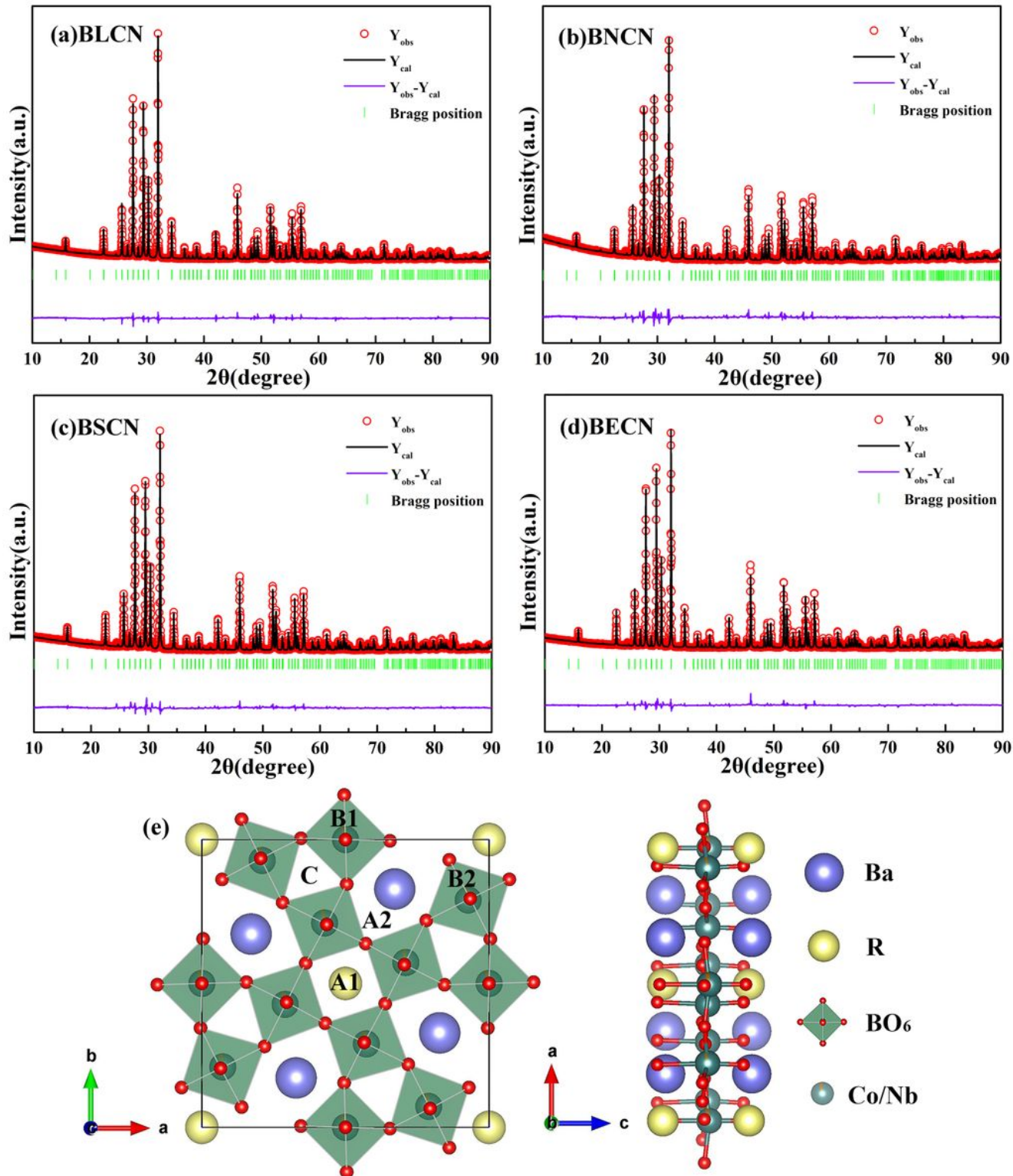
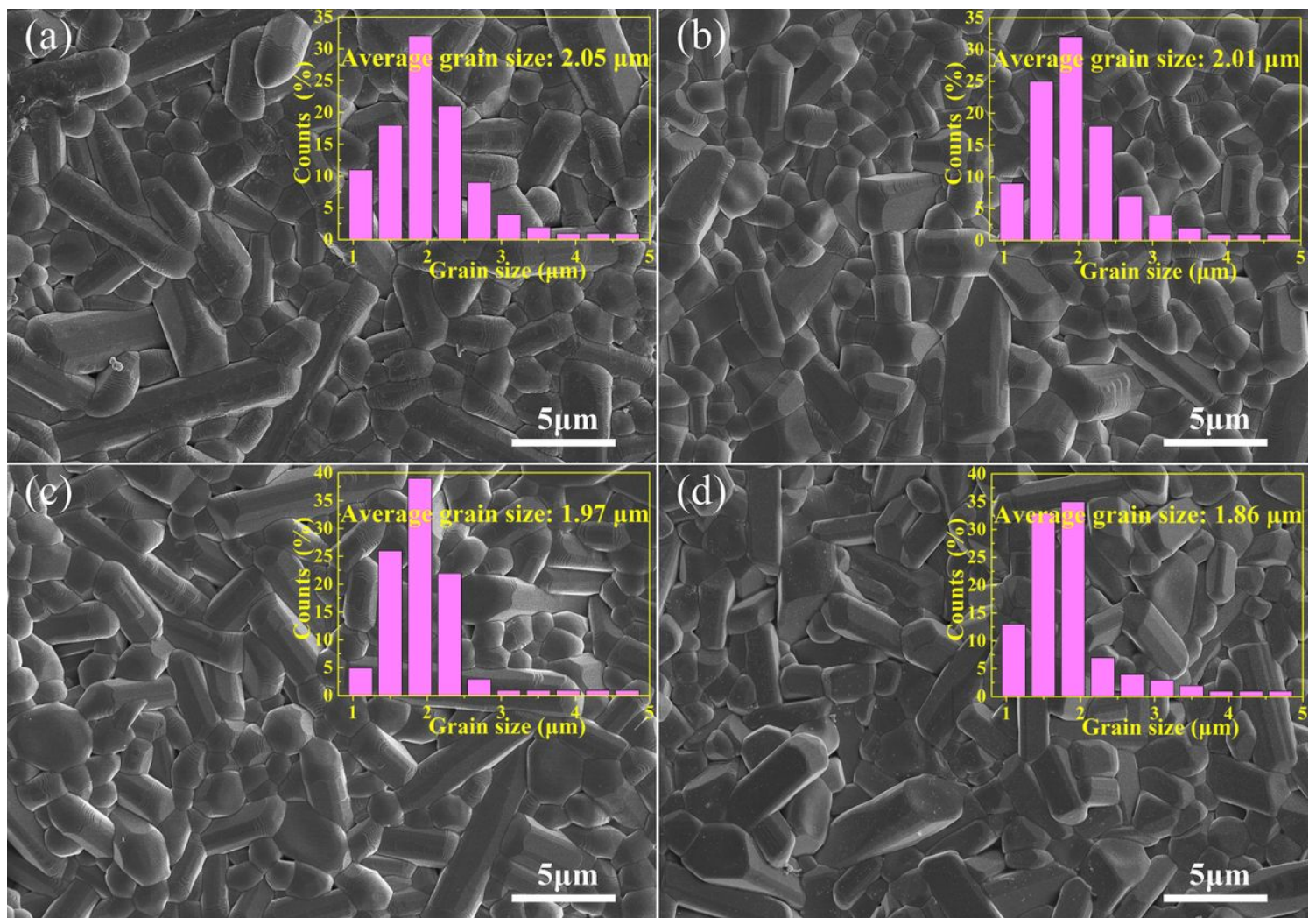


Figure 1

Refinement results of the (a)  $\text{Ba}_4\text{LaCo0.5Nb9.5O}_{30}$ , (b)  $\text{Ba}_4\text{NdCo0.5Nb9.5O}_{30}$ , (c)  $\text{Ba}_4\text{SmCo0.5Nb9.5O}_{30}$ , (d)  $\text{Ba}_4\text{EuCo0.5Nb9.5O}_{30}$  ceramics. (e) The ab and ac schematic representation of tetragonal tungsten bronze structure.



**Figure 2**

SEM images of the (a) Ba4LaCo0.5Nb9.5O30, (b) Ba4NdCo0.5Nb9.5O30, (c) Ba4SmCo0.5Nb9.5O30, (d) Ba4EuCo0.5Nb9.5O30 ceramics.

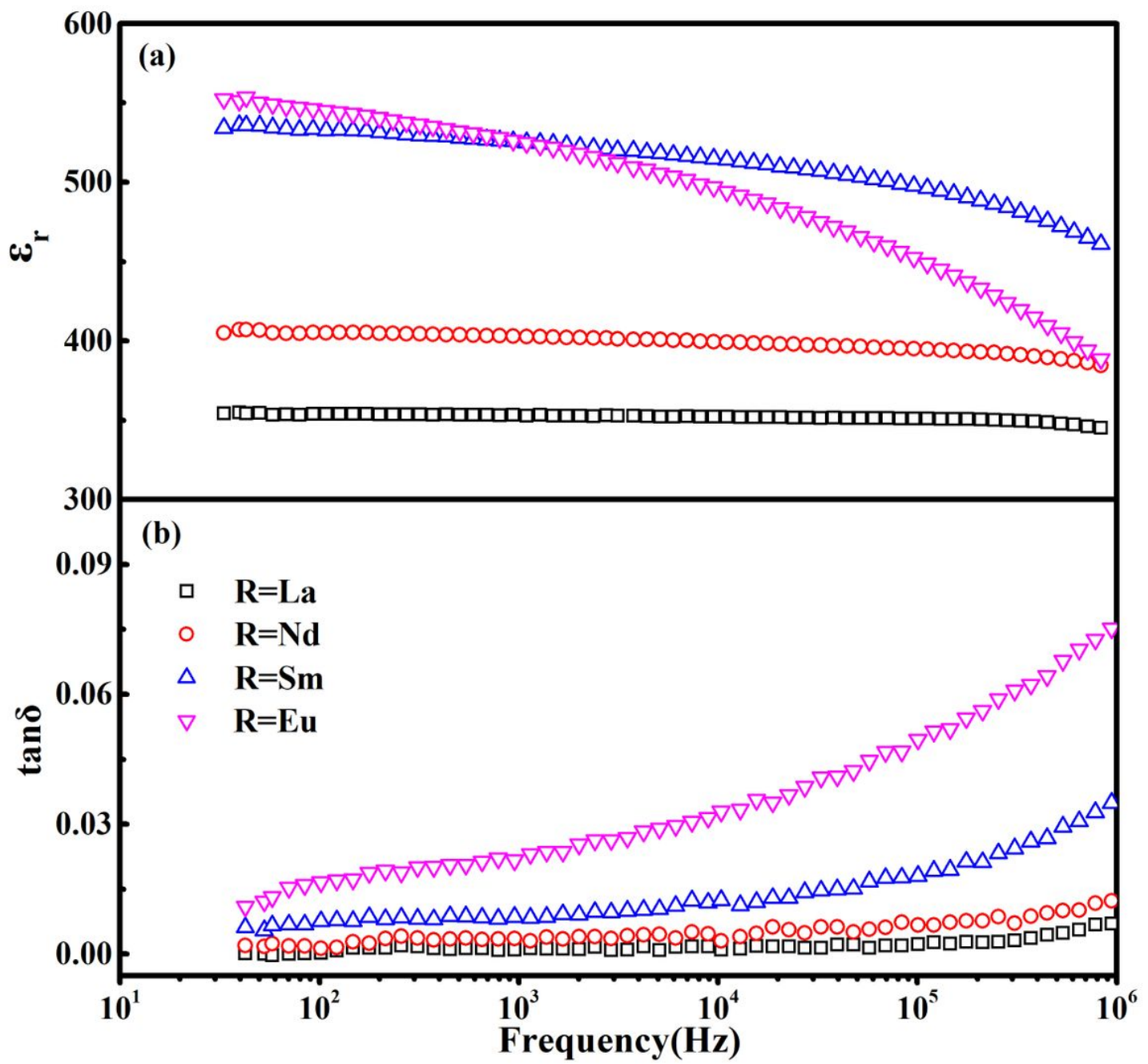


**Figure 3**

Frequency dependence dielectric properties of the  $\text{Ba}_4\text{RCo}_{0.5}\text{Nb}_{9.5}\text{O}_{30}$  ( $\text{R} = \text{La}, \text{Nd}, \text{Sm}, \text{Eu}$ ) ceramics.

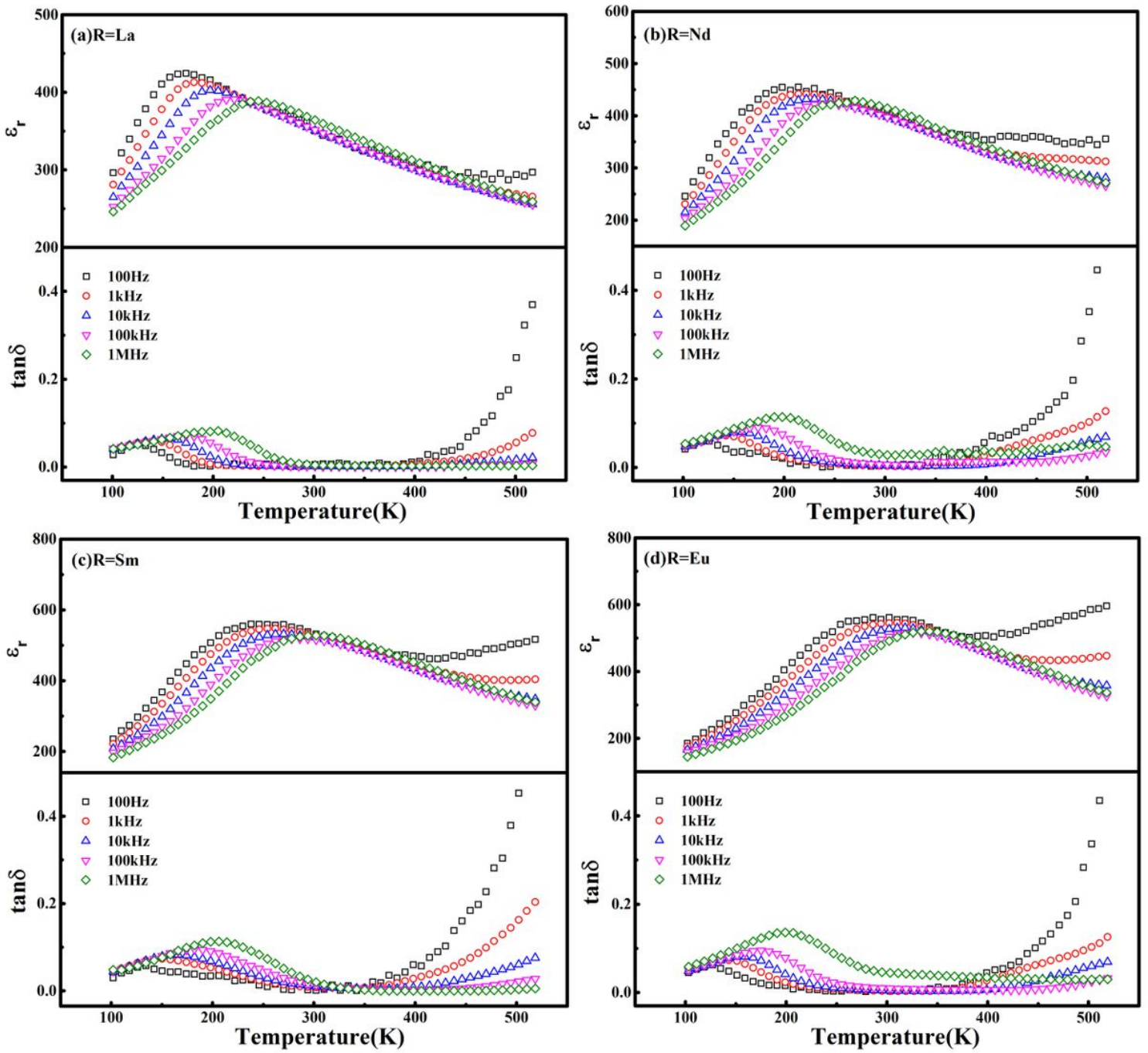


**Figure 4**

Temperature dependence of dielectric constant ( $\epsilon_r$ ) and dielectric loss ( $\tan\delta$ ) of the (a) Ba4LaCo0.5Nb9.5O30, (b) Ba4NdCo0.5Nb9.5O30, (c) Ba4SmCo0.5Nb9.5O30, and (d) Ba4EuCo0.5Nb9.5O30 ceramics.

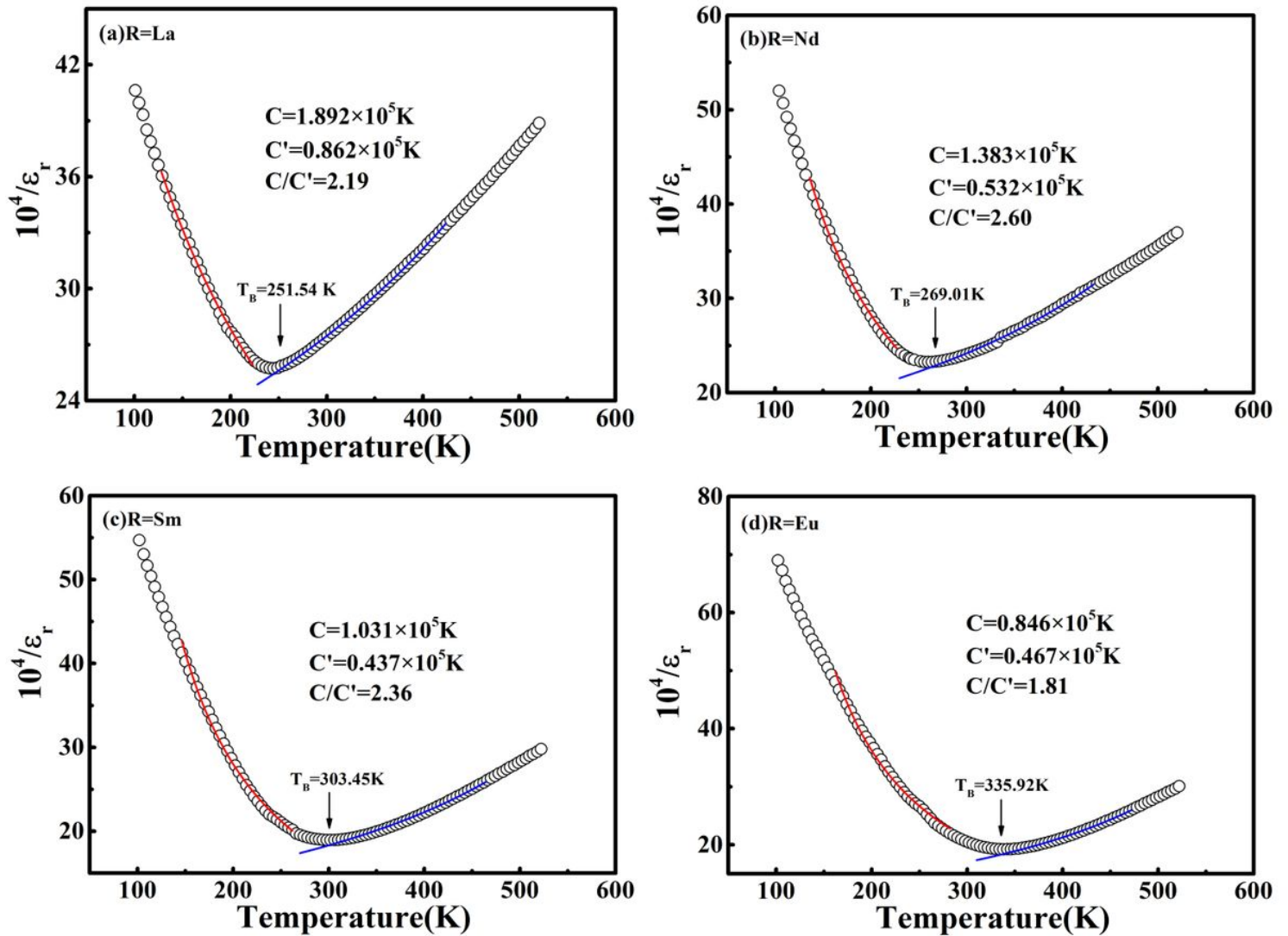


**Figure 5**

Curie-Weiss fitting of dielectric constant of the (a) Ba<sub>4</sub>LaCo0.5Nb9.5030, (b) Ba<sub>4</sub>NdCo0.5Nb9.5030, (c) Ba<sub>4</sub>SmCo0.5Nb9.5030, and (d) Ba<sub>4</sub>EuCo0.5Nb9.5030 ceramics measured at 1 MHz (experimental data: symbols; fitting result: lines).

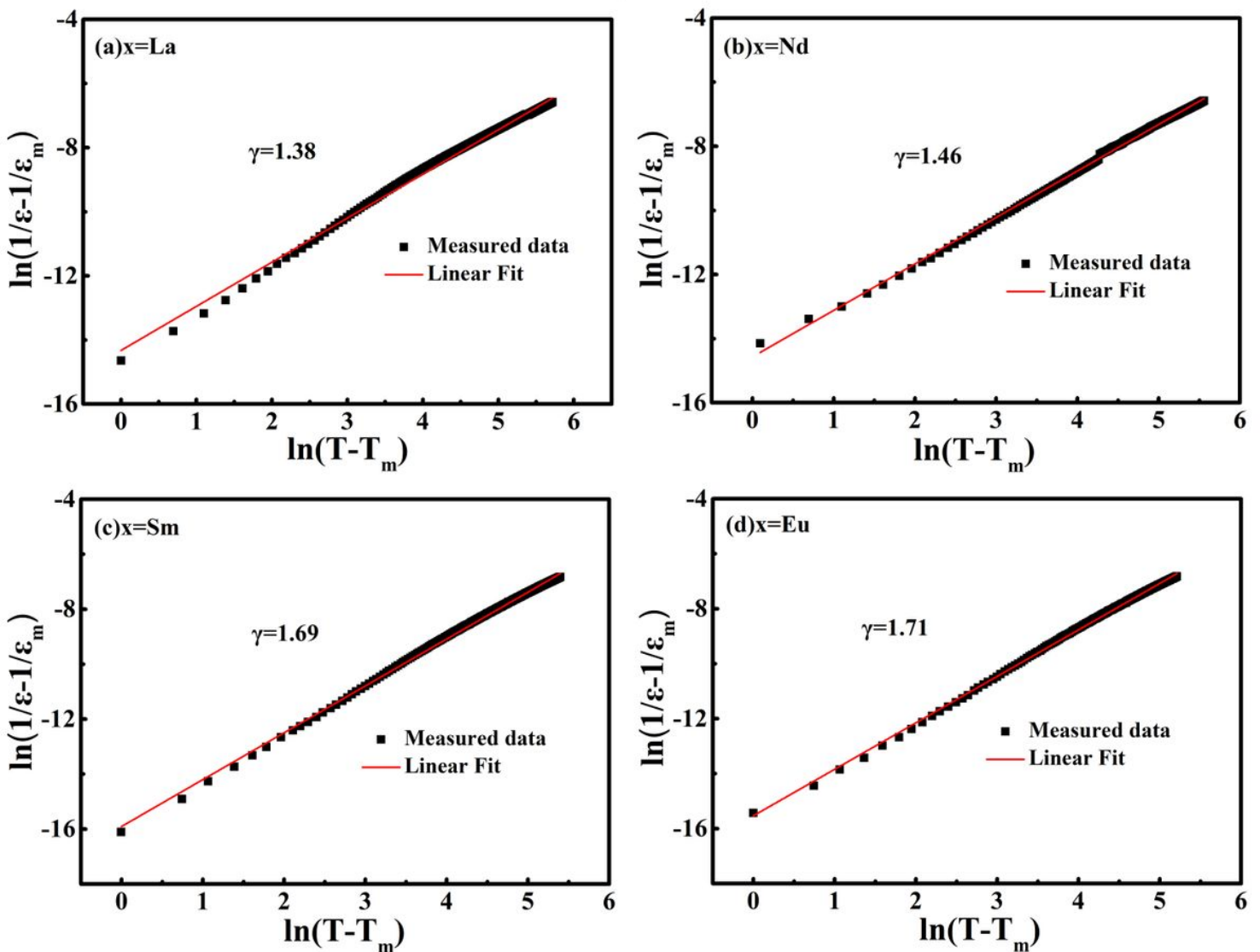


**Figure 6**

The Vogel-Fulcher fittings of  $\ln(1/\varepsilon - 1/\varepsilon_m)$  as a function of  $\ln(T - T_m)$  for the (a) Ba<sub>4</sub>LaCo0.5Nb9.5O<sub>30</sub>, (b) Ba<sub>4</sub>NdCo0.5Nb9.5O<sub>30</sub>, (c) Ba<sub>4</sub>SmCo0.5Nb9.5O<sub>30</sub>, and (d) Ba<sub>4</sub>EuCo0.5Nb9.5O<sub>30</sub> ceramics.

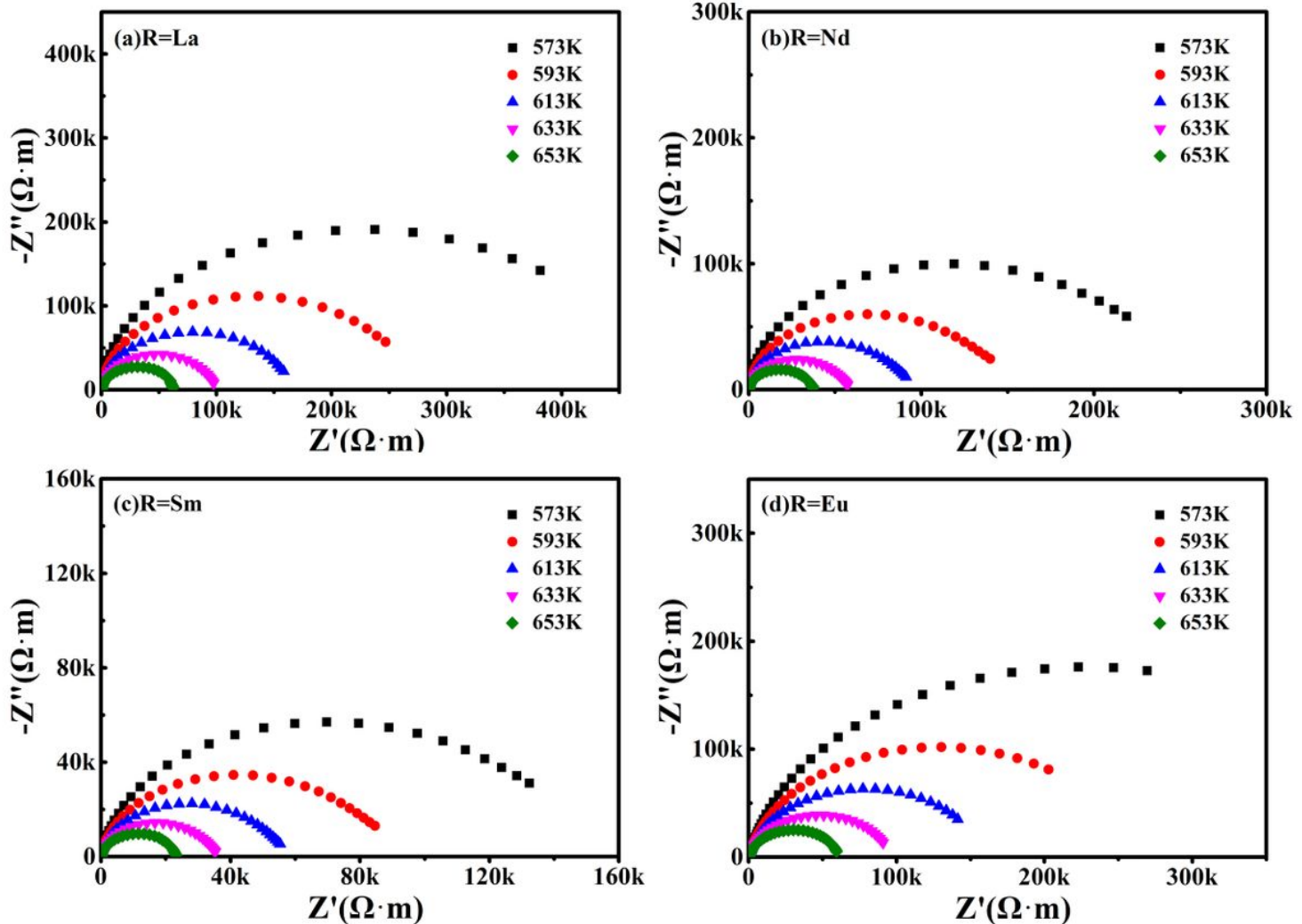


**Figure 7**

Complex impedance plots of the (a) Ba4LaCo0.5Nb9.5030, (b) Ba4NdCo0.5Nb9.5030, (c) Ba4SmCo0.5Nb9.5030, and (d) Ba4EuCo0.5Nb9.5030 ceramics at different temperatures.

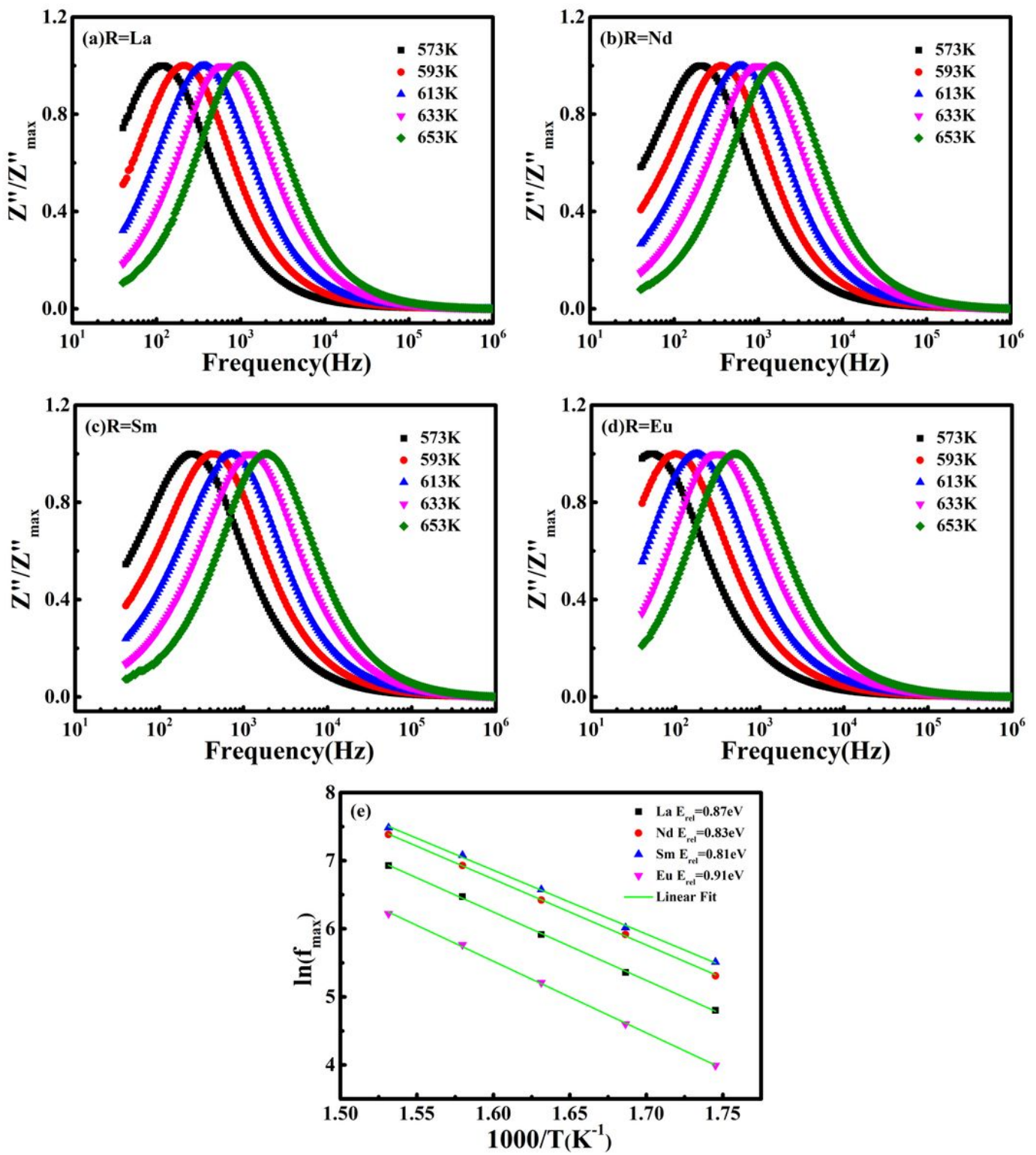


**Figure 8**

Normalized imaginary parts,  $Z''/Z''_{\max}$  of impedance at different frequency for the (a) Ba4LaCo0.5Nb9.5030, (b) Ba4NdCo0.5Nb9.5030, (c) Ba4SmCo0.5Nb9.5030, and (d) Ba4EuCo0.5Nb9.5030 ceramics. (e) Arrhenius plots of the relaxation frequencies ( $f_{\max}$ ) of the Ba4RCo0.5Nb9.5030 (R = La, Nd, Sm and Eu) ceramics. experimental data: symbols; fitting result: lines.

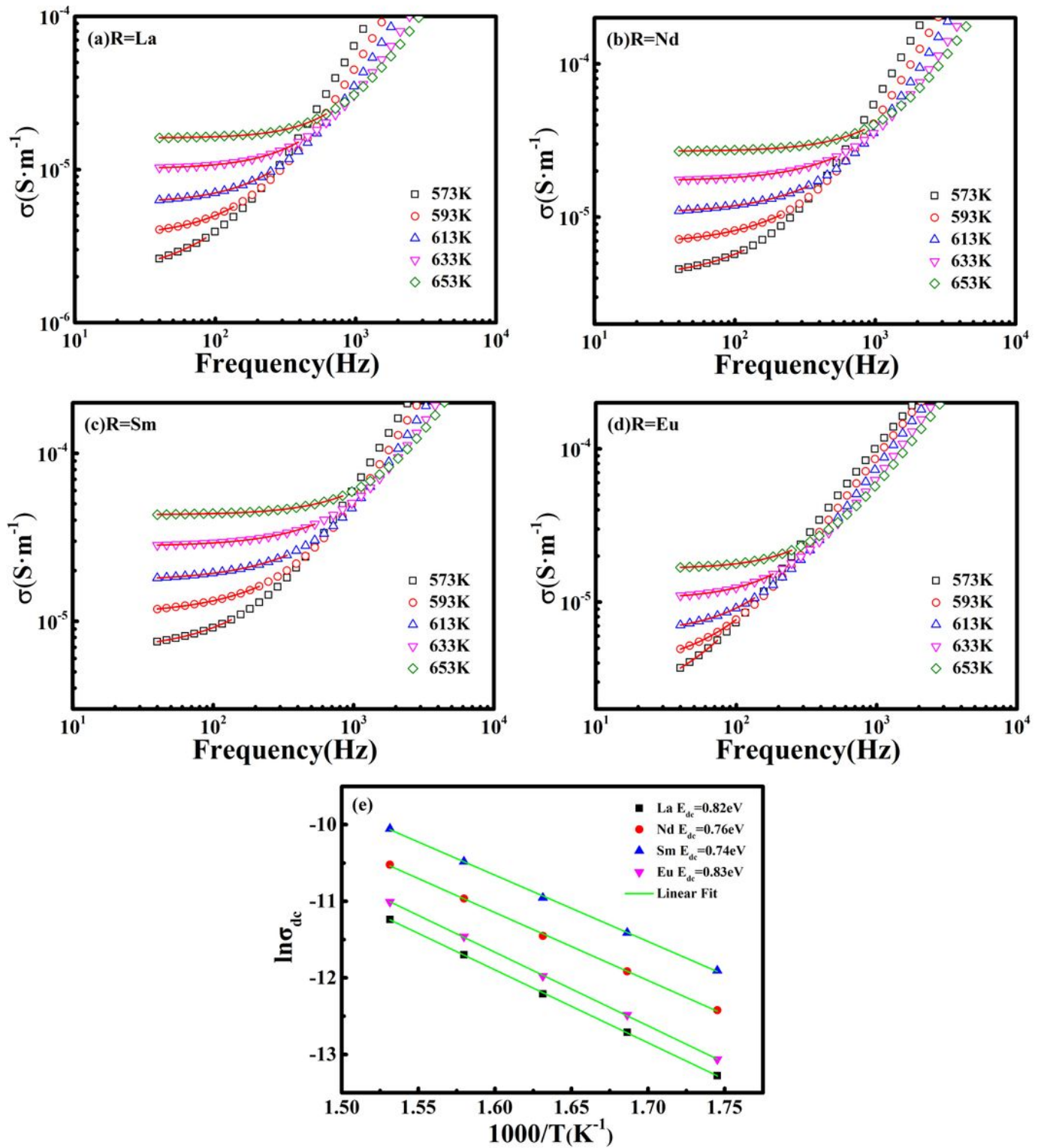


**Figure 9**

AC conductivity ( $\sigma_{ac}$ ) at different temperatures of the (a)  $\text{Ba}_4\text{LaCo}_{0.5}\text{Nb}_{9.5}\text{O}_{30}$ , (b)  $\text{Ba}_4\text{NdCo}_{0.5}\text{Nb}_{9.5}\text{O}_{30}$ , (c)  $\text{Ba}_4\text{SmCo}_{0.5}\text{Nb}_{9.5}\text{O}_{30}$ , and (d)  $\text{Ba}_4\text{EuCo}_{0.5}\text{Nb}_{9.5}\text{O}_{30}$  ceramics; the frequency dependence of the (e) DC conductivity ( $\sigma_{dc}$ ) obtained from fitting universal Arrhenius to the AC conductivity.

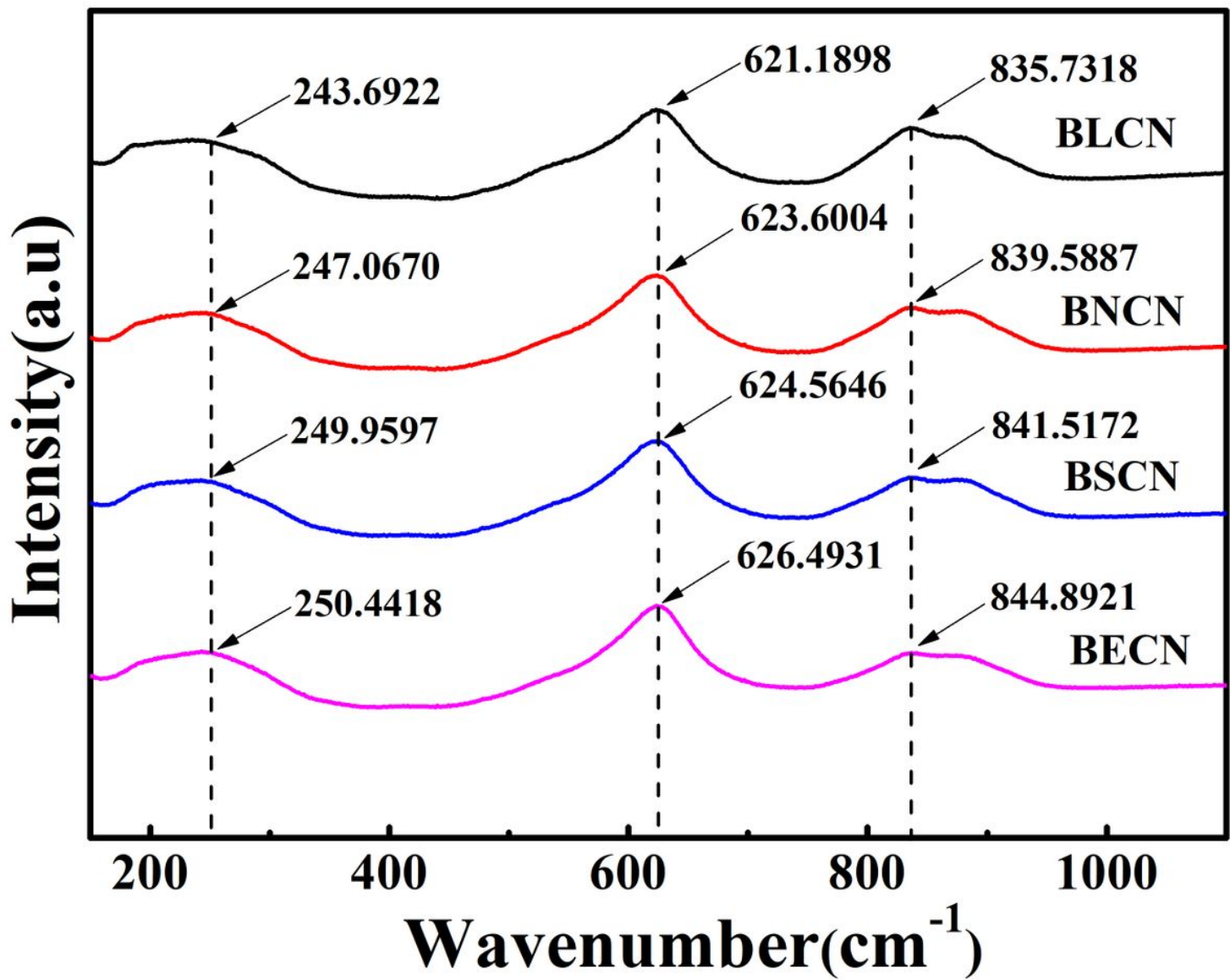
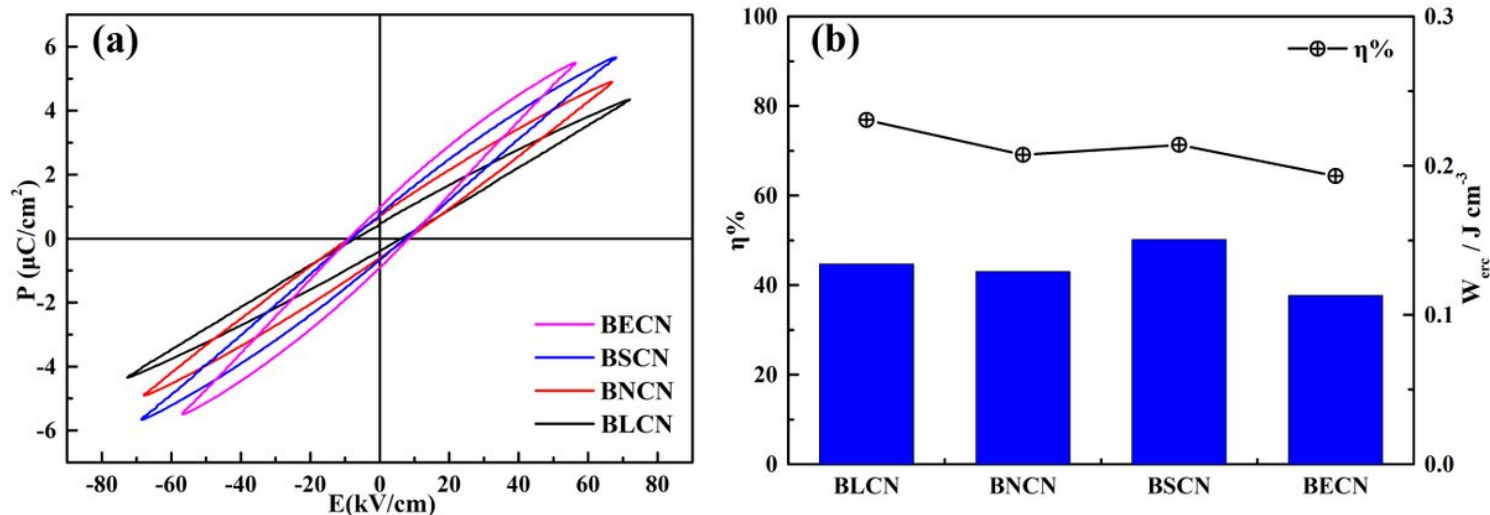


Figure 10

Raman spectra of the  $\text{Ba}_4\text{RCo}_0.5\text{Nb}_{9.5}\text{O}_{30}$  ( $\text{R} = \text{La, Nd, Sm and Eu}$ ) ceramics at room temperature.



## **Figure 11**

- (a) P-E curve of Ba<sub>4</sub>RCo<sub>0.5</sub>Nb<sub>9.5</sub>O<sub>30</sub> (R = La, Nd, Sm and Eu) ceramics under maximum field strength.  
(b) Energy storage efficiency and energy storage density of ceramics.